

Article

Utilizing a Tunable Delay Line Interferometer to Improve the Sensing Accuracy of an FBG Sensor System

Erfan Dejbani¹, Cheng-Kai Yao², Yibeltal Chanie Manie², Po-Yang Huang², Hao-Kuan Lee², Tan-Hsu Tan¹ and Peng-Chun Peng^{2,*}

¹ Department of Electrical Engineering, National Taipei University of Technology, Taipei 10608, Taiwan

² Department of Electro-Optical Engineering, National Taipei University of Technology, Taipei 10608, Taiwan

* Correspondence: pcpeng@ntut.edu.tw; Tel.: +886-2-2771-2171 (ext. 4671)

Abstract: This paper proposes a novel sensing system based on a tunable delay line interferometer. The tunable delay line interferometer has been used to interpret strain, bringing us high accuracy as well as tunability. The shifted wavelength of the fiber Bragg grating (FBG) sensor caused by the applied strain can be visualized by an optical power meter (OPM) instead of an optical spectrum analyzer (OSA) by converting it to a power change using a tunable delay line interferometer (TDI). Different free spectral ranges (FSRs) are assigned to the TDI to investigate the accuracy and operation range of the proposed system. Thus, we achieve high accuracy and sensitivity by adjusting the FSR to 0.47 nm. Experimental results show that the maximum output power variation corresponding to a strain of 10 $\mu\epsilon$ is about 0.9 dB when the FSR is set to 0.47 nm. The proposed system is also cost-effective regarding the equipment utilized for interrogation: a tunable delay line interferometer and an optical power meter.

Keywords: tunable delay line interferometer; fiber Bragg grating (FBG) sensor; sensing system



Citation: Dejbani, E.; Yao, C.-K.; Manie, Y.C.; Huang, P.-Y.; Lee, H.-K.; Tan, T.-H.; Peng, P.-C. Utilizing a Tunable Delay Line Interferometer to Improve the Sensing Accuracy of an FBG Sensor System. *Photonics* **2022**, *9*, 869. <https://doi.org/10.3390/photonics9110869>

Received: 30 September 2022

Accepted: 14 November 2022

Published: 17 November 2022

Publisher's Note: MDPI stays neutral with regard to jurisdictional claims in published maps and institutional affiliations.



Copyright: © 2022 by the authors. Licensee MDPI, Basel, Switzerland. This article is an open access article distributed under the terms and conditions of the Creative Commons Attribution (CC BY) license (<https://creativecommons.org/licenses/by/4.0/>).

1. Introduction

Roughly all aspects of communication technology nowadays have undergone a revolution with the introduction of fiber-optic transmission. In recent years, numerous studies have been conducted based on optical fiber sensors for a variety of purposes, including the measurement of strain and temperature [1–4], vibration [5], electric current [6], pressure [7], and liquid level [8]. Among the variety of fiber optic sensors, the fiber Bragg grating (FBG)-based sensors have advantages due to their ability to perform the basic functions of reflection, dispersion, and filtering that are commonly used in sensing applications. Since the discovery of FBG [9] and the theory of sensor sensitivities presented in [10], it has become a hot topic in the field of optical sensing due to FBG's inherent benefits such as compact size, real-time response, high accuracy, high sensitivity, low cost, and immunity to electromagnetic interference [11]. By employing grating-based devices, it is possible to sense a wide range of parameters [12]. Thus, there are numerous domains where fiber Bragg gratings are currently used, including high-temperature sensors, health and biomedical equipment, structural engineering, biochemical applications, radioactive environments, and marine and civil engineering [13–16]. Although there has been substantial progress in monitoring different environmental parameters using FBG sensors, it is still difficult to interrogate the reflected wavelength because doing so increases both complexity and expense.

The primary principle of interrogating the FBG response is based on scanning the reflected wavelength. Therefore, either a broadband light source that covers the entire measurement band or a tunable narrowband laser is used as the light source. Thus, after determining the central wavelength, the shift of the central wavelength can be interpreted as environmental changes, such as temperature, strain, and other external information, which

form the basis of the sensing principle of the FBG sensor. In order to provide successful monitoring in different applications, the establishment of an FBG-based monitoring system entails the appropriate design of the sensing system, reasonable implementation, and FBG sensor packing technology [11]. For instance, in [17], simultaneous discrimination of temperature and strain changes using the FBG sensor was proposed. In [18], a combination of polymer planar and Bragg grating was proposed as a tensile and compressive strain sensor. Recently, to achieve an ideal monitoring system, a new approach using a 3D printer [19] was proposed to improve the FBG sensor for achieving a linearity of greater than 98%, a sensitivity of about 0.7 pm/N, and an ability to withstand a force of 1 kN. However, the criteria of precisely identifying the small and dynamic fluctuations of the FBG's central wavelength cannot be addressed by standard spectrum interrogation techniques such as using an optical spectrum analyzer (OSA) with low resolution and response speed. Therefore, finding an FBG interrogation technique that has a high resolution and a fast response time is crucial. This particular field has been the subject of a lot of studies recently, including fiber grating filters [20–23] and filters of interferometers [24–27], which require complex setups and highly skilled craftsmanship to make the fiber filters, and the accuracy cannot be adjusted promptly. In [28], using arrayed waveguide grating (AWG) as a demultiplexer of multiple FBGs and an array of edge filters to accurately interrogate the wavelength shift of FBGs was proposed. They monitor each FBG separately, using two adjacent channels of the AWG. Although this method reduces costs and has acceptable accuracy, and a neural network can improve the wavelength interrogation range [29], the accuracy is constant. Furthermore, a novel ultra-compact photonic tuneable notch filter with a flat-bottom passband was proposed in [30]. Nonetheless, connecting this type of filter to an FBG sensor requires a precise design of the connection between filter and sensor, or the operating range of the FBG cannot be covered. Thus, it is necessary to consider a sensing system that is both cost-effective and tunable for different purposes. As a result, it is essential to develop new ways of decoding wavelength-encoded signals and converting them into readable and efficient ones.

In this paper, to the best of our knowledge, we propose a new sensing system based on the tunable delay line interferometer (TDI), where the accuracy and operating range of the system can be adjusted by tuning the free spectral range (FSR) of the TDI. To achieve higher accuracy, the TDI is set at a lower FSR so that a slight shift of the FBG center wavelength causes a significant change in the power value. In contrast, to have a wider operating range, the TDI is set at a higher FSR. However, to have high accuracy when using an interferometer with a low FSR, which leads to a narrow operating range, an FBG with a narrow reflection response is required. Thus, among the different FBG sensors, such as uniform, chirped, and tilted superstructures, the FBG sensor with uniform fiber grating was chosen in this study. The proposed system is cost-effective since we used mainly a TDI and an optical power meter (OPM) as components of the measurement system. The advantage of the OPM-based system over an OSA-based system is the quicker response speed. Additional benefits of the TDI system over other homemade interferometer-based methods are high tunability and efficiency. Moreover, the FSR of the fiber optic interferometer in other similar experimental setups is difficult to reach at 0.4 nm when compared to this proposed scheme. Therefore, the proposed structure gains some advantages over other fiber optic interferometer-based sensors. The main novelty of the proposed system can be highlighted as follows:

- Our proposed system is tunable according to the tunability of the TDI;
- Compared with other systems, the proposed system is cost-effective because interrogation of FBG reflection spectra requires only the OPM and no other expensive equipment;
- Since the interrogation of the system and the measurement of various parameters can be performed by the TDI and OPM in the sensing center or the central office, the proposed system is portable.

2. Experimental Setup

Figure 1 depicts the proposed experimental setup, a conceptual schematic of the internal structure of the TDI, and a conceptual schematic of the reflection response of the strain that was applied to the FBG before and after passing through the TDI. In this setup, the broadband light source (BLS) of 14.95 dBm is fed to the FBG through an optical circulator (OC). The FBG sensor will reflect a Gaussian wave whose central wavelength will be shifted according to the applied strain. The reflected wave is then fed into the TDI, which demodulates the wavelength shift into the power change for detection by the OPM, and the components of the TDI are sealed in an iron box to prevent the internal components from the external ambient. The inner TDI consists of two plate beam splitters and a triangular prism, creating an optical path difference and causing interference, while a mirror on the other side is positioned to create a phase difference that splits two outputs by nearly 180 degrees. The FSR tunable interference of the TDI is formed by a tunable triangular prism using the tunable micrometer knob of the TDI, which can adjust the delay path length of the TDI, as shown in the lower-left corner of Figure 1. Figure 2a shows the two outputs of the TDI, which have a phase difference of 180 degrees and can be thought of as the power filter. In Figure 2b, output 2 shows four different FSRs (4.79 nm, 2.38 nm, 1.61 nm, and 0.71 nm). It can be observed that by decreasing the FSR, the rising/falling slope of the interference pattern will change. Thus, the slope change of the operating range gives us different accuracies. However, the FSR can be tuned to a higher value in cases requiring a more comprehensive operating range. Moreover, under different FSRs, the lobe crests or lobe troughs of the interference pattern can be adjusted to the same wavelength position to match the wavelength of the same FBG.

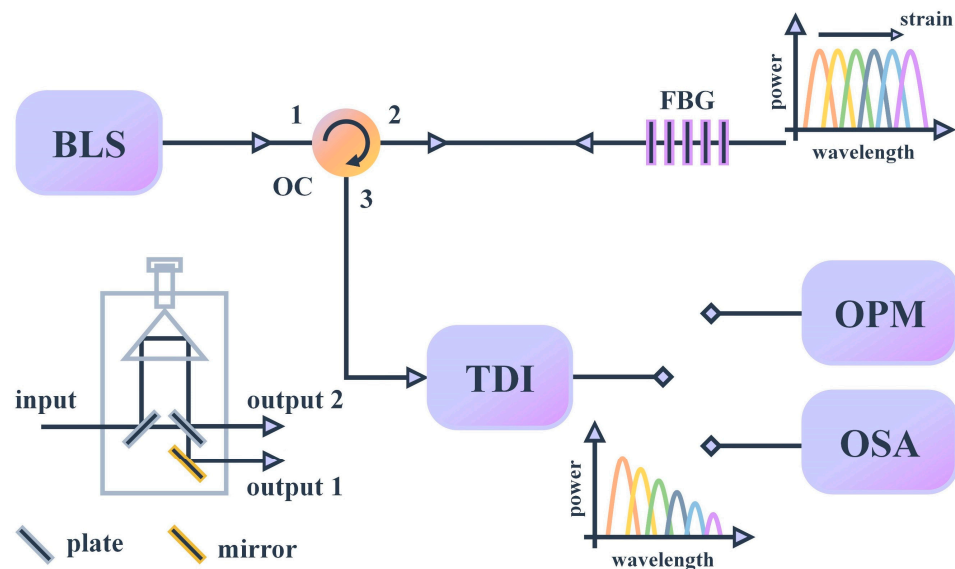


Figure 1. The proposed experimental setup and internal structure of the tunable delay line interferometer. The data acquisition in the experimental setup was made by first connecting outputs 1 and 2 of the tunable delay line interferometer (TDI) to the optical power meter (OPM) and optical spectrum analyzer (OSA) to measure power and record the spectra, then connecting output 2 to the OPM to measure power. The broadband light source (BLS) feeds the fiber Bragg grating (FBG) strain sensor through the optical circulator (OC). The reflected wave is modulated by a TDI and detected by an OPM and an OSA. The wavelengths and power changes of the FBG without and after the TDI under different strains are shown in the upper and lower right corners, respectively.

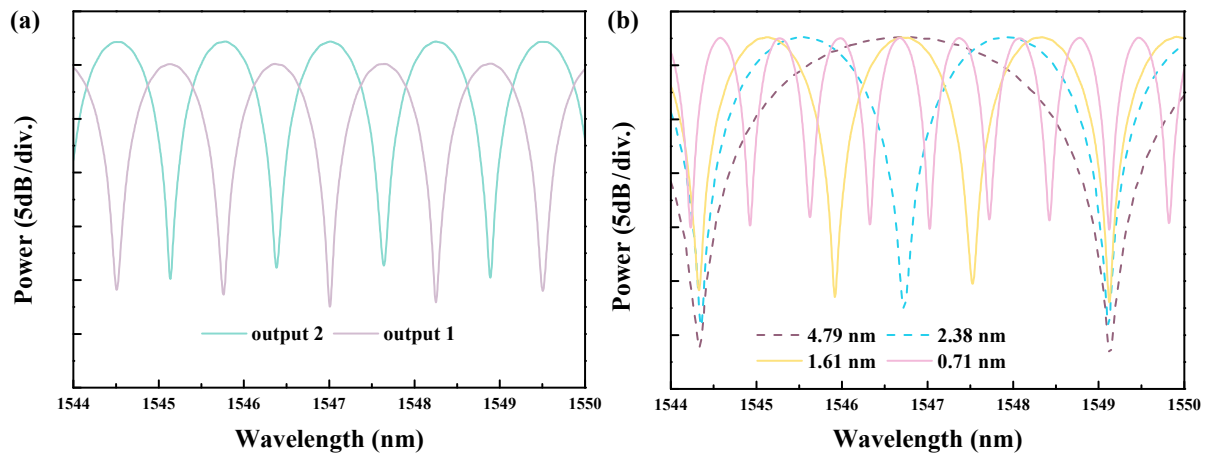


Figure 2. (a) The outputs of the TDI based on output 1 and output 2 (b) the TDI output for different FSR values using output 1.

In this paper, different strains were applied to the FBG sensor to shift the central wavelength. The FBGs are light-reflecting structures that reflect Gaussian light at particular wavelengths while transmitting the rest of the light spectrum. The peak wavelength of the reflected spectrum from a single sensor, the Bragg wavelength (λ_B), is the center of the Gaussian reflected spectrum. The Bragg uniform structure can define the Bragg wavelength [31].

$$\lambda_B = 2\eta_{eff}\Lambda \tag{1}$$

In Equation (1), the η_{eff} and Λ are the effective index and period of the grating, respectively. The FBG sensor’s Bragg wavelength shifts as it is strained. A shift in the Bragg wavelength is the result of a change in FBG length that has occurred from either compressive or tensile strain, which affects the period of the grating (Λ). The equation below shows the relation between wavelength change and strain [32]:

$$\Delta\lambda_B = \lambda_B \times (1 - \rho\varepsilon) \times \varepsilon_m \tag{2}$$

where $\rho\varepsilon$ is the photo-elastic coefficient of the fiber, $\varepsilon_m = \Delta L/L$ is the mechanical strain, and L is the fixed length of FBG. Thus, the strain applied to the FBG can be interpreted as a shift of the Bragg wavelength, and therefore the FBG wavelength shift superimposed on the interference pattern of the TDI leads to a decrease/increase of the power intensity, as demonstrated in the next section. The central wavelength of the FBG tested in this paper is shifted to about 1 pm for each microstrain applied. In this paper, the FBG optical long-gauge sensor (FS310) used was a commercial device purchased from 3L Technologies Inc. (Taiwan), which is a fiber Bragg grating (FBG) sensor with a durable and flexible polymer tube. The delay line interferometer under test in this study is a Kylaia WT-MINT, which enables setting the delay of the interferometer to the required value via a micrometer head.

3. Results and Discussion

Nevertheless, it is not desirable to interpret the FBG response through the OSA. Here we just use it to illustrate how different FSRs lead to different accuracy and operating ranges. Therefore, one output of the TDI was connected to the OSA, and the FBG sensor was set to a Bragg wavelength of 1545 nm. Afterward, five different strains were applied to the FBG to cover the operating range. According to Figure 2, the reflected wavelength of the FBG can be shifted within the operating range, which starts from the peak and ends at the valley of the TDI interference. Therefore, reducing the FSR leads to a reduction in the operating range, which means that the bandwidth of the lobe is reduced, and the slope of the filter increases. Figure 3 shows the OSA outputs of five different strain steps ($s_0, s_1, s_2, s_3,$ and s_4) for five different FSR values.

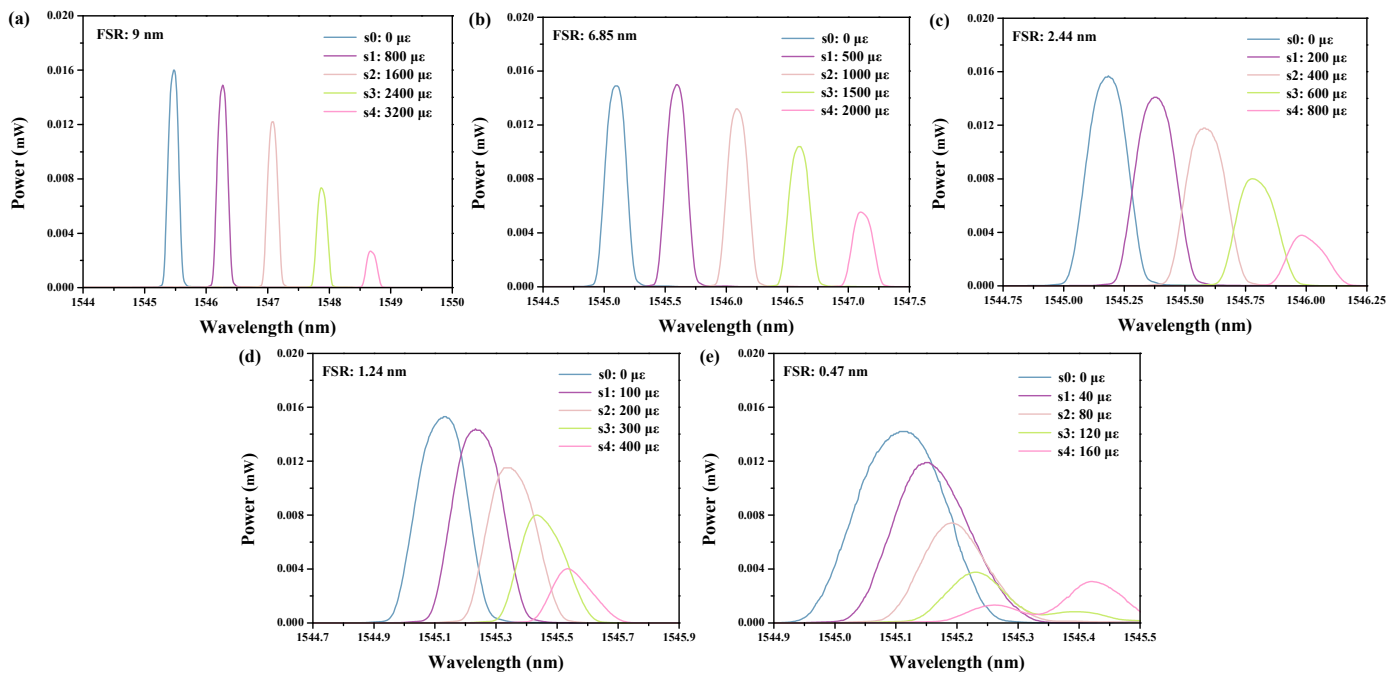


Figure 3. From (a–e), FBG is subjected to strain variation spectra with FSR of 9 nm, 6.85 nm, 2.44 nm, 1.24 nm, and 0.47 nm for the TDI, where the strain size is set according to the magnitude of the FSR.

In Figure 3a, the FSR is set to 9 nm, which has a high operating range, and a strain of 800 $\mu\epsilon$ is applied at each step of the wavelength, resulting in a variation of the output power. As can be seen from Figure 3a–e, the accuracy is significantly improved by reducing the FSR from 9 nm to 0.47 nm. It should be noted that in Figure 3e, the operating range is reduced so that the trade-off between accuracy and operating range can be adjusted according to the requirements of different applications. As mentioned before, using the OSA to interrogate a sensing system is not desirable according to its limitations in accuracy and response time. Hence, the modulated wavelength shift is changed into optic power that is measured by the OPM. In Figure 4, the output power is depicted versus the different strains at the same number of steps. It should be noted that for different FSRs (according to Figure 3) we applied the same number of steps, but different steps of strains for different FSRs. For example, for the 9 nm FSR the strain increases by 800 $\mu\epsilon$ for each step (purple line with square point), while for the 0.47 nm FSR the strain increases by 40 $\mu\epsilon$ for each step (blue line with triangular point). Figure 4a,b show the measured values of the two outputs of the TDI, which correspond to the same strain ratios for the different FSR settings in Figure 3a–e, respectively. For example, at FSRs of 0.47 nm, 1.24 nm, and 2.44 nm, the wavelength drift caused by the applied strain is close to two-thirds of half the FSR. Therefore, it can be seen from Figure 4a,b that the optical power curves of 1.24 nm and 2.44 nm FSR are close to each other, while the FSR of 0.47 nm cannot be close to them because the bandwidth of the FBG exceeds 0.47 nm and crosses to another lobe that can be observed from Figure 3e. For example, the wavelength drift caused by the applied strain was less than and more than two-thirds of half the FSR for FSR settings of 6.85 nm and 9 nm, respectively. Therefore, the slope of the power variation curve for the 6.85 nm FSR is slightly smaller than that of other FSRs, as can be seen from step 0 to step 2 of Figures 3b and 4b, and the slope of the power variation curve for the 9 nm FSR is also slightly larger than that of other FSRs, as can be seen from the step 2 to 4 of Figure 4b. This means that the measurement under this system is very accurate, and the power variation can be completely mapped to the different interference patterns at different FSRs.

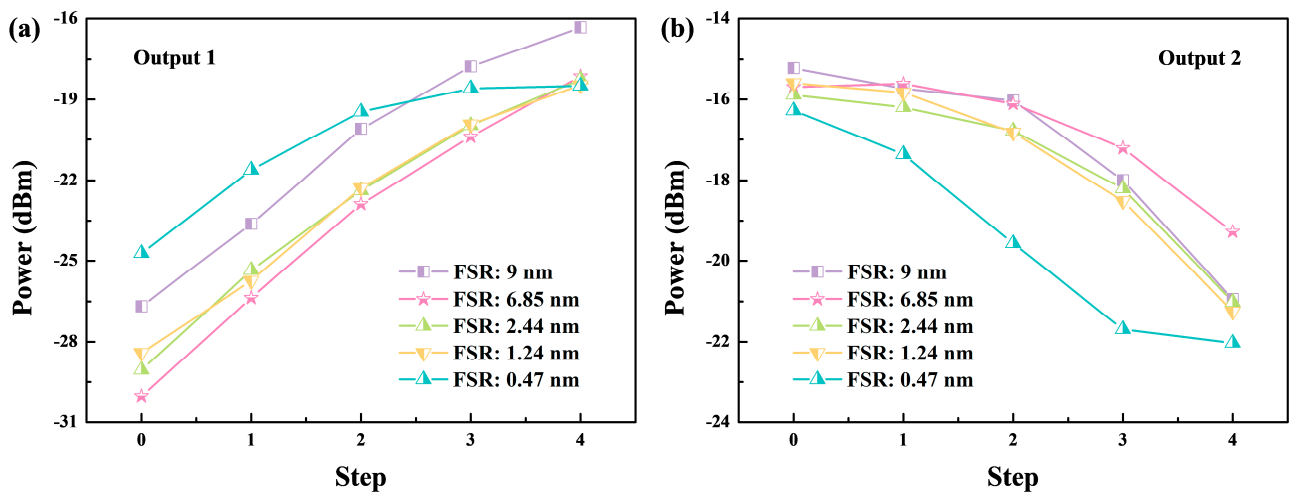


Figure 4. The power variation curves in the same number of steps via the results of Figure 3, where the FSR of the TDI and the strain applied to each step are 800 $\mu\epsilon$ strain for 9 nm FSR, 500 $\mu\epsilon$ strain for 6.85 nm FSR, 200 $\mu\epsilon$ strain for 2.44 nm FSR, 100 $\mu\epsilon$ strain for 1.24 nm FSR, and 40 $\mu\epsilon$ strain for 0.47 nm FSR. (a) When the power change is measured from the TDI output 1, the FBG is strained from the lobe trough where the slope is large until the FBG wavelength shifts to about two-thirds of the FSR half (b) when the power change is measured from the TDI output 2, the FBG is strained from the lobe peak where the slope is small until the FBG wavelength shifts to about two-thirds of the FSR half.

It is also worth mentioning that since the phases of the two outputs of the TDI are orthogonal, the power measurement of output 1 in Figure 4a starts from the bottom of the lobe, corresponding to the larger slope shown in Figure 2b. Since the power variation between the two outputs of the TDI is different, with output 1 taking a path from the lobe valley to the lobe slope change area and output 2 taking a path from the lobe crest to the lobe slope change area, one of the two outputs can be used as a reference to monitor the measurement accuracy of the other output. Incidentally, if we need to measure a larger parameter of environmental variation and do not need the interference pattern of the two slope curves, we can also adjust the FSR of the TDI to about 20 nm, then the power variation measured by the conventional FBG will have only one slope. In addition, it can be seen from Figure 4a that the power variation is significantly smaller than in other FSR settings when the FSR is 0.47 nm, which is because the value of the FSR is proportional to the extinction ratio, as shown in Figure 2b, where the lobe bottom power level rises at an FSR of 0.47 nm. Given the problem that the 40 microstrains per step applied at 0.47 nm FSR were too large to prevent the FBG from crossing to another lobe, another experiment was supplemented at 0.47 nm FSR to obtain maximum accuracy.

In this experiment, output 1 of the TDI was connected to the OPM, and output 2 of the TDI was connected to the OSA. After this, a minimum strain (10 $\mu\epsilon$) was applied to the FBG using our test equipment. Figure 5a shows the change in the output power of output 1 of the TDI in these ten steps. In Figure 5b, output 2 of the TDI obtained from the OSA is plotted as ten strain steps, and since the strain only varies from 0 $\mu\epsilon$ to 90 $\mu\epsilon$, the power of the FBG will not significantly be shifted to the next lobe. Thus, in the FSR of 0.47 nm, we achieved a strain of 10 $\mu\epsilon$, corresponding to a maximum output power variation of about 0.9 dB. For the most part, the characteristics of most fiber optic interferometers make it difficult to achieve an FSR of 0.4 nm and retain an extinction ratio of more than 15 dB [33,34], but in our proposed system, we achieved high-precision sensor signals with FSR values of 0.47 nm and extinction ratios close to 20 dB. In this study, FSR values higher than 0.47 nm were chosen to show different accuracy and operating ranges depending on the operating range of the FBG sensor. However, different FSRs can also be applied by controlling the micrometer knob of the TDI according to the designed application preference. Furthermore,

unless the FSR is adjusted a great amount, the power variation of the FBG under this system will be consistent with the curve of the interference pattern of the TDI, and it is difficult to achieve perfect linearity. Fortunately, we have previously accomplished the use of machine learning to predict the strain on the FBG wavelengths under different FBG superimpositions [2,35]. Therefore, the same concept of utilizing machine learning can be used to solve the problem that the power variation of this system does not show perfect linearity, which affects the determination of how much strain is applied.

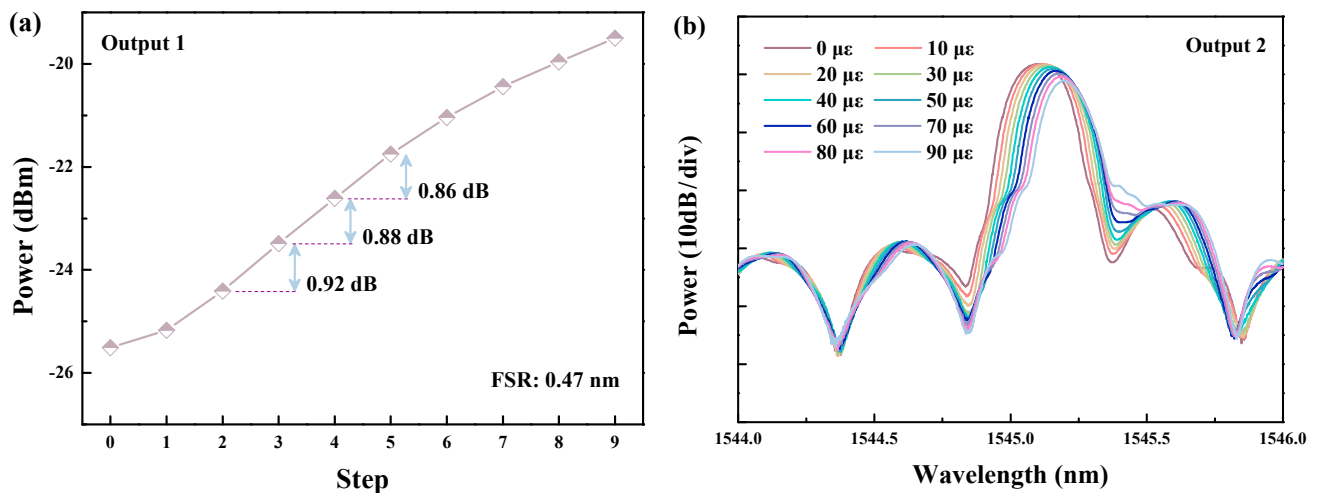


Figure 5. (a) Power variation at output 1 of the TDI, where the FBG is subjected to a strain of $10 \mu\epsilon$ per step, with strains corresponding to $0 \mu\epsilon$ to $90 \mu\epsilon$ from step 0 to step 9. (b) spectral variation at output 2 of the TDI, where the FBG is subjected to a strain of $10 \mu\epsilon$ per step, with strains corresponding to $0 \mu\epsilon$ to $90 \mu\epsilon$.

4. Conclusions

In this paper, we proposed a new sensing system based on a tunable delay line interferometer (TDI) for high-precision interrogation of a fiber Bragg grating (FBG) strain sensor. Moreover, the proposed system is tunable, which brings more freedom for different applications by adjusting the accuracy and operating range. Depending on the characteristics of the TDI, the free spectral range (FSR) can be tuned, allowing the sensing system to realize different accuracies. To achieve higher accuracy, the TDI is set at a lower FSR so that a slight shift of the central wavelength of the FBG leads to a significant change in the power value. It should be noted that simultaneously achieving both an FSR of 0.4 nm and a good extinction ratio for significant variation in power is a hard task for other similar experimental devices, such as fiber optic interferometers. Furthermore, the proposed system is cost-effective since we use only a light source, a TDI, and an optical power meter (OPM) as components of the measurement system. Therefore, the proposed structure gains some advantages over other fiber optic interferometer-based sensors.

Author Contributions: Conceptualization, E.D., C.-K.Y., Y.C.M. and P.-C.P.; methodology, E.D., C.-K.Y. and Y.C.M.; data preparation, E.D., C.-K.Y., P.-Y.H. and H.-K.L.; model validation, E.D., C.-K.Y. and Y.C.M.; formal analysis, P.-Y.H., H.-K.L., T.-H.T. and P.-C.P.; investigation, E.D., C.-K.Y., Y.C.M., P.-Y.H., H.-K.L., T.-H.T. and P.-C.P. All authors have read and agreed to the published version of the manuscript.

Funding: This work was supported by the Ministry of Science and Technology, Taiwan, under Grant MOST 110-2221-E-027-035-MY2.

Data Availability Statement: Not applicable.

Conflicts of Interest: The authors declare no conflict of interest.

References

1. Ramakrishnan, M.; Rajan, G.; Semenova, Y.; Farrell, G. Overview of Fiber Optic Sensor Technologies for Strain/Temperature Sensing Applications in Composite Materials. *Sensors* **2016**, *16*, 90. [\[CrossRef\]](#)
2. Chiu, P.H.; Lin, Y.S.; Manie, Y.C.; Li, J.W.; Lin, J.H.; Peng, P.C. Intensity and Wavelength-Division Multiplexing Fiber Sensor Interrogation Using a Combination of Autoencoder Pre-Trained Convolution Neural Network and Differential Evolution Algorithm. *IEEE Photonics J.* **2021**, *13*, 1–9. [\[CrossRef\]](#)
3. Hayle, S.T.; Manie, Y.C.; Yao, C.K.; Yeh, T.Y.; Yu, C.H.; Peng, P.C. Hybrid of Free Space Optics Communication and Sensor System Using IWDM Technique. *J. Light. Technol.* **2022**, *40*, 5862–5869. [\[CrossRef\]](#)
4. Bao, Y.; Huang, Y.; Hoehler, M.S.; Chen, G. Review of Fiber Optic Sensors for Structural Fire Engineering. *Sensors* **2019**, *19*, 877. [\[CrossRef\]](#)
5. Du, C.; Dutta, S.; Kurup, P.; Yu, T.; Wang, X. A Review of Railway Infrastructure Monitoring Using Fiber Optic Sensors. *Sens. Actuators A Phys.* **2020**, *303*, 111728. [\[CrossRef\]](#)
6. Eftimov, T.A.; Dyankov, G.L.; Kolev, P.; Vladev, V.P. A Simple Fiber Optic Magnetic Field and Current Sensor with Spectral Interrogation. *Opt. Commun.* **2022**, *527*, 128930. [\[CrossRef\]](#)
7. Tavares, C.; Domingues, M.F.; Paixão, T.; Alberto, N.; Silva, H.; Antunes, P. Wheelchair pressure ulcer prevention using FBG based sensing devices. *Sensors* **2019**, *20*, 212. [\[CrossRef\]](#)
8. Rajamani, A.S.; Divagar, M.; Sai, V.V.R. Plastic Fiber Optic Sensor for Continuous Liquid Level Monitoring. *Sens. Actuators A Phys.* **2019**, *296*, 192–199. [\[CrossRef\]](#)
9. Hill, K.O.; Meltz, G. Fiber Bragg Grating Technology Fundamentals and Overview: Fiber Gratings, Photosensitivity, and Poling. *J. Light. Technol.* **1997**, *15*, 1263–1276. [\[CrossRef\]](#)
10. Lukosz, W.; Tiefenthaler, K. Sensitivity of Grating Couplers as Integrated-Optical Chemical Sensors. *J. Opt. Soc. Am. B* **1989**, *6*, 209–220. [\[CrossRef\]](#)
11. Hong, C.Y.; Zhang, Y.F.; Zhang, M.X.; Leung, L.M.G.; Liu, L.Q. Application of FBG Sensors for Geotechnical Health Monitoring, a Review of Sensor Design, Implementation Methods and Packaging Techniques. *Sens. Actuators A Phys.* **2016**, *244*, 184–197. [\[CrossRef\]](#)
12. Chen, J.; Liu, B.; Zhang, H. Review of Fiber Bragg Grating Sensor Technology. *Front. Optoelectron. China* **2011**, *4*, 204–212. [\[CrossRef\]](#)
13. Mieloszyk, M.; Ostachowicz, W. An Application of Structural Health Monitoring System Based on FBG Sensors to Offshore Wind Turbine Support Structure Model. *Mar. Struct.* **2017**, *51*, 65–86. [\[CrossRef\]](#)
14. Kaur, G.; Kaler, R.S. Investigate the Optical FBG Sensor to Monitor Displacement and Vibration in Civil Structure. *Opt. Quantum. Electron.* **2022**, *54*, 121. [\[CrossRef\]](#)
15. Min, R.; Liu, Z.; Pereira, L.; Yang, C.; Sui, Q.; Marques, C. Optical Fiber Sensing for Marine Environment and Marine Structural Health Monitoring: A Review. *Opt. Laser Technol.* **2021**, *140*, 107082. [\[CrossRef\]](#)
16. Riza, M.A.; Go, Y.I.; Harun, S.W.; Maier, R.R.J. FBG Sensors for Environmental and Biochemical Applications—A Review. *IEEE Sens. J.* **2020**, *20*, 7614–7627. [\[CrossRef\]](#)
17. Annunziato, A.; Anelli, F.; Gates, J.; Holmes, C.; Prudenziato, F. Design of Polarization-Maintaining FBGs Using Polyimide Films to Improve Strain-Temperature Sensing in CFRP Laminates. *IEEE Photonics J.* **2021**, *13*, 7100315. [\[CrossRef\]](#)
18. Schmauss, B.; Hessler, S.; Belle, S.; Rosenberger, M.; Hellmann, R. Compressive and Tensile Strain Sensing Using a Polymer Planar Bragg Grating. *Opt. Express* **2014**, *22*, 5483–5490. [\[CrossRef\]](#)
19. Leal-Junior, A.G.; Marques, C.; Ribeiro, M.R.N.; Pontes, M.J.; Frizzera, A. FBG-Embedded 3-D Printed ABS Sensing Pads: The Impact of Infill Density on Sensitivity and Dynamic Range in Force Sensors. *IEEE Sens. J.* **2018**, *18*, 8381–8388. [\[CrossRef\]](#)
20. Potts, C.; Allen, T.W.; Azar, A.; Melnyk, A.; Dennison, C.R.; DeCorby, R.G. Wavelength Interrogation of Fiber Bragg Grating Sensors Using Tapered Hollow Bragg Waveguides. *Opt. Lett.* **2014**, *39*, 5941–5944. [\[CrossRef\]](#)
21. Fernández, M.P.; Bulus Rossini, L.A.; Cruz, J.L.; Andrés, M.V.; Costanzo Caso, P.A. High-Speed and High-Resolution Interrogation of FBG Sensors Using Wavelength-to-Time Mapping and Gaussian Filters. *Opt. Express* **2019**, *27*, 36815–36823. [\[CrossRef\]](#) [\[PubMed\]](#)
22. Sun, Y.; Yao, Y.; Niu, H.; Zha, H.; Zhang, L.; Tian, Z.; Chen, N.K.; Ren, Y. Peak wavelength and bandwidth tunable fiber Bragg grating notch filter induced by femtosecond laser point by point inscription. *Opt. Commun.* **2022**, *521*, 128583. [\[CrossRef\]](#)
23. Kim, D.K.; Kim, J.; Lee, S.-L.; Choi, S.; Jeong, S.J.; Kim, M.S.; Lee, Y.W. Simultaneous Measurement of Strain and Temperature Using Long-Period Fiber Grating Written on Polarization-Maintaining Photonic Crystal Fiber. *J. Nanosci. Nanotechnol.* **2020**, *20*, 257–262. [\[CrossRef\]](#)
24. Yang, G.; Guo, J.; Xu, G.; Lv, L.; Tu, G.; Xia, L. A Novel Fiber Bragg Grating Wavelength Demodulation System Based on F-P Etalon. In Proceedings of the Optoelectronic Devices and Integration V, SPIE, Beijing, China, 9–11 October 2014; Volume 9270, p. 92700V.
25. Das, B.; Chandra, V. Fiber-MZI-Based FBG Sensor Interrogation: Comparative Study with a CCD Spectrometer. *Appl. Opt.* **2016**, *55*, 8287–8292. [\[CrossRef\]](#) [\[PubMed\]](#)
26. Diaz, C.A.; Marques, C.A.; Domingues, M.F.F.; Ribeiro, M.R.; Frizzera-Neto, A.; Pontes, M.J.; André, P.S.; Antunes, P.F. A cost-effective edge-filter based FBG interrogator using catastrophic fuse effect micro-cavity interferometers. *Measurement* **2018**, *124*, 486–493. [\[CrossRef\]](#)

27. Wei, L.; Khattak, A.; Martz, C.; Zhou, D.P. Tunable multimode fiber based filter and its application in cost-effective interrogation of fiber-optic temperature sensors. *IEEE Photonics J.* **2017**, *9*, 1–8. [[CrossRef](#)]
28. Su, H.; Huang, X.G. A Novel Fiber Bragg Grating Interrogating Sensor System Based on AWG Demultiplexing. *Opt. Commun.* **2007**, *275*, 196–200. [[CrossRef](#)]
29. Chen, S.; Yao, F.; Ren, S.; Wang, G.; Huang, M. Cost-effective improvement of the performance of AWG-based FBG wavelength interrogation via a cascaded neural network. *Opt. Express* **2022**, *30*, 7647–7663. [[CrossRef](#)]
30. Brunetti, G.; Dell’olio, F.; Conteduca, D.; Armenise, M.N.; Ciminelli, C. Ultra-Compact Tuneable Notch Filter Using Silicon Photonic Crystal Ring Resonator. *J. Light. Technol.* **2019**, *37*, 2970–2980. [[CrossRef](#)]
31. Majumder, M.; Gangopadhyay, T.K.; Chakraborty, A.K.; Dasgupta, K.; Bhattacharya, D.K. Fibre Bragg Gratings in Structural Health Monitoring-Present Status and Applications. *Sens. Actuators A Phys.* **2008**, *147*, 150–164. [[CrossRef](#)]
32. Li, R.; Chen, Y.; Tan, Y.; Zhou, Z.; Li, T.; Mao, J. Sensitivity Enhancement of FBG-Based Strain Sensor. *Sensors* **2018**, *18*, 1607. [[CrossRef](#)] [[PubMed](#)]
33. Miliou, A. In-Fiber Interferometric-Based Sensors: Overview and Recent Advances. *Photonics* **2021**, *8*, 265. [[CrossRef](#)]
34. Chen, Y.; Zhao, L.; Hao, S.; Tang, J. Advanced Fiber Sensors Based on the Vernier Effect. *Sensors* **2022**, *22*, 2694. [[CrossRef](#)] [[PubMed](#)]
35. Manie, Y.C.; Yao, C.-K.; Yeh, T.-Y.; Teng, Y.-C.; Peng, P.-C. Laser based optical wireless communications for the Internet of Things (IoT) Application. *IEEE Internet Things J.* **2022**. [[CrossRef](#)]